PCCP

Accepted Manuscript




ROYAL SOCIETY OF CHEMISTRY

www.rsc.org/pccp

Journal Name

ARTICLE

# Pt-functionalized $Fe_2O_3$ photoanodes for solar water splitting: the role of hematite nano-organization and platinum redox state†

Received 00th January 20xx,
Accepted 00th January 20xx

DOI: 10.1039/x0xx00000x

www.rsc.org/

M. E. A. Warwick,[a] D. Barreca,[b] E. Bontempi,[c] G. Carraro,[a] A. Gasparotto,[*a] C. Maccato,[a] K. Kaunisto,[ad] T.-P. Ruoko,[d] H. Lemmetyinen,[d] C. Sada,[e] Y. Gönüllü,[f] and S. Mathur[f]

Pt/α-$Fe_2O_3$ nanocomposites were synthesized on fluorine-doped tin oxide (FTO) substrates by a sequential plasma enhanced-chemical vapor deposition (PE-CVD)/radio frequency (RF) sputtering approach, tailoring the overall Pt content as a function of sputtering time. The chemico-physical properties of the as-prepared systems were extensively investigated by means of complementary techniques, including X-ray diffraction (XRD), X-ray photoelectron spectroscopy (XPS), field emission-scanning electron microscopy (FE-SEM), energy dispersive X-ray spectroscopy (EDXS), secondary ion mass spectrometry (SIMS), and optical absorption spectroscopy, and compared to those of the homologous Pt/α-$Fe_2O_3$ systems annealed in air prior and/or after sputtering. The obtained results evidenced that the material compositional, structural and morphological features, with particular regard to Pt oxidation state and *hematite* nano-organization, could be finely tailored as a function of the adopted processing conditions. Pt/α-$Fe_2O_3$ systems were finally tested as photoanodes in photoelectrochemical (PEC) water splitting experiments, evidencing a remarkable interplay between functional performances and the above material properties, as also evidenced by transient absorption spectroscopy (TAS) results.

## Introduction

Photoelectrochemical (PEC) water splitting is a promising and environmentally benign method to convert solar energy into hydrogen, an attractive fuel with a high energy density and a clean combustion.[1-3] The key component of a PEC cell is the photoanode, typically consisting of an *n*-type metal oxide (*e.g.* $TiO_2$, ZnO, $WO_3$ or $Fe_2O_3$) promoting the oxygen evolution reaction (OER) at the semiconductor-liquid junction (SCLJ).[2,4-7] Among the possible anode materials, α-$Fe_2O_3$ (*hematite*) is considered an appealing candidate for the fabrication of Vis-light absorbing photoelectrodes, thanks to its band-gap of 2.0-2.2 eV as well as to its large abundance, low cost, non-toxicity and chemical stability in aqueous media.[1,3,5,8,9] In spite of these important advantages, *hematite* also presents some critical drawbacks that detrimentally affect its photoefficiency, among which a low absorption coefficient ($\alpha^{-1}$ = 118 nm at λ = 550 nm), poor electrical conductivity and short hole diffusion length (*L* = 2-4 nm).[1,4,7,8,10,11] In fact, the large difference between $\alpha^{-1}$ and *L* values results in the recombination of many charge carriers generated far from the SCLJ, producing, in turn, a detrimental performance degradation.[4]

To circumvent these problems, recent studies have focused on strategies to decouple photon harvesting and charge carrier exploitation. In this context, the fabrication of nanomaterials with tailored structure and morphology is commonly adopted to shorten the pathway that photoexcited holes ($h^+$) have to travel to reach the SCLJ,[1,3,6,8,10-12] whereas the improvement of crystallinity and tailoring of crystallographic orientation can enhance charge transport properties.[7] The control of α-$Fe_2O_3$ nano-organization might also result in a more efficient light harvesting, provided that a proper tuning in particle size, shape, and defect content is achieved.[8,13,14] Furthermore, as the nanostructure size shrinks down, the total surface area exposed to the electrolyte and the density of reaction sites available on the semiconductor surface undergo an increase, with a beneficial effect on the ultimate PEC behavior.[2,3,8,12]

Other successful approaches to tune *hematite* properties involve either doping (for instance by $Mg^{2+}$, $Zn^{2+}$, $Si^{+4}$, $Sn^{4+}$, $Ti^{4+}$, $Pt^{4+}$) or functionalization with nanoparticles (NPs, *e.g.* Ir, Pt, Au, $RuO_2$).[2-4,9,13] In this regard, elemental doping of α-$Fe_2O_3$ has been reported to increase its electrical conductivity, enhance its optical absorption coefficient, catalytically improve the OER surface kinetics and, in some cases, also favourably affect the system morphology and surface area.[1,3,6,7,9,11] In addition, heterocomposite electrodes can yield improved functional performances through the exploitation of various phenomena (*e.g.* catalytic, electronic, plasmonic). For instance, heterojunction formation in composite photocatalysts results in the generation of an internal electric field that extends the lifetime of electron-hole ($e^-/h^+$) pairs and limits recombination

[a] *Department of Chemistry, Padova University and INSTM, 35131 Padova, Italy. * Corresponding author E-mail: alberto.gasparotto@unipd.it*
[b] *CNR-IENI and INSTM, Department of Chemistry, Padova University, 35131 Padova, Italy*
[c] *Chemistry for Technologies Laboratory, Brescia University, 25123 Brescia, Italy*
[d] *Department of Chemistry and Bioengineering, Tampere University of Technology, 33101 Tampere, Finland*
[e] *Department of Physics and Astronomy, Padova University, 35131 Padova, Italy*
[f] *Department of Chemistry, Chair of Inorganic and Materials Chemistry, Cologne University, 50939 Cologne, Germany*

† Electronic supplementary information (ESI) available: Experimental details on the adopted synthesis and characterization techniques as well as additional FE-SEM, AFM, XRD, XPS and TAS data on Pt/α-$Fe_2O_3$ nanocomposites. See DOI: 10.1039/x0xx00000x

losses, promoting thus the target redox reactions.[2,4,13,15]

Basing on the above observations, we report herein on the plasma enhanced-chemical vapor deposition (PE-CVD) fabrication of α-$Fe_2O_3$ nanostructures, their modification by Pt sputtering and eventual annealing in air. Although other researchers previously focused on the preparation of Pt/α-$Fe_2O_3$ electrodes for PEC water splitting,[5,7,9,16,17] the number of literature reports on this subject is relatively limited and further studies are necessary to clarify the actual role of *hematite* nanostructure/morphology, as well as platinum loading and oxidation state,[9,13] that strongly depend on the adopted processing route. In this work, thanks to a multi-technique characterization approach, we show that variations in the annealing procedure (carried out either before and/or after Pt deposition) enable an efficient tailoring of the composition, nano-organization and optical properties of the resulting Pt/α-$Fe_2O_3$ heterocomposites, yielding a remarkable improvement of PEC behavior in water splitting. Transient absorption spectroscopy (TAS) has been used to investigate charge carrier dynamics in the target photoanodes, showing a clear interplay between charge recombination kinetics and PEC efficiency.[11,18,19]

## Experimental

### Synthesis

$Fe_2O_3$ deposits were fabricated by means of a two-electrode radio frequency (RF, ν = 13.56 MHz) PE-CVD apparatus described elsewhere.[20] Growth experiments were performed from $Ar/O_2$ plasmas on FTO-coated glass slides using $Fe(hfa)_2$TMEDA (hfa = 1,1,1,5,5,5-hexafluoro-2,4-pentanedionate; TMEDA = *N*,*N*,*N*',*N*'-tetramethylethylenediamine) as iron precursor,[21] under the following conditions: growth temperature = 300 °C; RF-power = 10 W; total pressure = 1.0 mbar; process duration = 1 h.

Platinum sputtering on iron oxide samples was carried out from Ar plasmas in the same reactor used for PE-CVD experiments (growth temperature = 60 °C; RF-power = 5 W; total pressure = 0.3 mbar) using two different sputtering times (30 or 50 min).

Finally, the obtained samples were *ex-situ* annealed in air for 1 h using a Carbolite HST 12/200 tubular oven prior and/or after sputtering (see Table 1) at a fixed temperature of 650 °C.

### Characterization

2D X-ray microdiffraction ($XRD^2$) measurements were performed in reflection mode on a Dymax-RAPID X-ray microdiffractometer using CuKα radiation. Conventional XRD patterns were then obtained by integration of 2D images.

X-ray photoelectron spectroscopy (XPS) analyses were run on a Perkin-Elmer Φ 5600ci spectrometer using a standard AlKα radiation (1486.6 eV). The reported binding energies (BEs) were corrected for charging phenomena by assigning to the adventitious C1s signal a BE of 284.8 eV.[22]

Field emission-scanning electron microscopy (FE-SEM) micrographs were collected with a Zeiss SUPRA 40 VP instrument, equipped with an Oxford INCA x-sight X-ray detector for energy dispersive X-ray spectroscopy (EDXS) analyses.

Secondary ion mass spectrometry (SIMS) measurements were carried out by means of a IMS 4f mass spectrometer (Cameca) using a 14.5 keV $Cs^+$ primary beam and by negative secondary ion detection, adopting an electron gun for charge compensation.

Optical absorption spectra were recorded in transmission mode on a Cary 50 spectrophotometer. Optical band-gap energies ($E_G$) were evaluated by the Tauc formula:[17,21]

$$(\alpha h\nu)^n = A\,(h\nu - E_G) \quad (1)$$

where α is the absorption coefficient, hν is the incident photon energy, *A* is a constant, *n* is an exponent dependent on the nature of electronic transitions (*n* = 2 for *hematite* direct transitions).[8]

Photoelectrochemical (PEC) analyses were carried out in NaOH solutions (pH = 13.7), using a saturated calomel electrode (SCE) as a reference, a Pt wire as counter-electrode and the Pt/$Fe_2O_3$ nanodeposits as working electrodes. Linear sweep voltammetry was carried out in the potential range from -1 to 1 V *vs.* SCE using a potentiostat (PAR, Versa state IV) and a Xe lamp (150 W, Oriel) with an AM 1.5 filter. Potentials with respect to the reversible hydrogen electrode (RHE) scale were calculated using the Nernst equation:[11,12,23]

$$E_{RHE} = E_{SCE} + E^{\circ}_{SCE} + 0.059\ pH \quad (2)$$

Transient absorption spectroscopy (TAS) measurements were performed on samples with a geometric area of 3×3 $cm^2$ in a complete PEC cell (PECC-2, Zahner-elektrik). A standard three-electrode configuration was used having a Pt counter-electrode, an Ag/AgCl (3 M KCl) reference electrode and a 0.1 M NaOH electrolyte. A potential value of 1.6 V *vs.* RHE, set by a standard potentiostat (F02A, Faraday MP), was selected to study the charge dynamics at the SCLJ, since it provided an optimal signal-to-noise ratio.

More details on the adopted synthesis and characterization techniques are provided in the electronic supplementary information (ESI).

## Results and discussion

The Pt/$Fe_2O_3$ specimens investigated in the present work were synthesized using two different sputtering times (*i.e.* 30 or 50 min) to tailor the Pt loading. Moreover, samples were analyzed both prior and after air annealing, performing the thermal treatment step before and/or after Pt sputtering. While annealing prior to Pt deposition was expected to influence the morphological and structural features of the oxide matrix,[14] post-annealing of Pt/$Fe_2O_3$ samples could potentially affect the quality of Pt/$Fe_2O_3$ interface, as well as Pt dispersion and oxidation state(s).[5,7,9] The main preparative conditions adopted in the present work are summarized in Table 1.

| Sputtering time (min) | Sample label | Pre annealing | Post annealing | $x_{Pt}$ |
|---|---|---|---|---|
| 30 | Pt(30) | // | // | 80 |
| | A+Pt(30) | 650 °C | // | 80 |
| | Pt(30)+A | // | 650 °C | 60 |
| | A+Pt(30)+A | 650 °C | 650 °C | 30 |
| 50 | Pt(50) | // | // | 90 |
| | A+Pt(50) | 650 °C | // | 90 |
| | Pt(50)+A | // | 650 °C | 70 |
| | A+Pt(50)+A | 650 °C | 650 °C | 40 |

**Table 1** Preparative conditions for as-grown and annealed Pt/$Fe_2O_3$ nanocomposites. Surface platinum molar fraction, determined from XPS analyses, is defined as $x_{Pt}$ = [Pt/(Pt+Fe)]×100.

Fig. 1 compares representative $XRD^2$ maps of the as-prepared Pt/$Fe_2O_3$ sample containing the highest Pt amount (Fig. 1a) and of the homologous specimen obtained after a double annealing in air

(Fig. 1b). In both cases, no reflections from Pt-containing species were detected, likely due to the relatively low overall platinum content and the reduced size of Pt-based aggregates (see below). Conversely, diffraction peaks from the α-$Fe_2O_3$ (*hematite*) phase could be clearly appreciated in the XRD[2] images, along with the signals of the underlying FTO substrate.

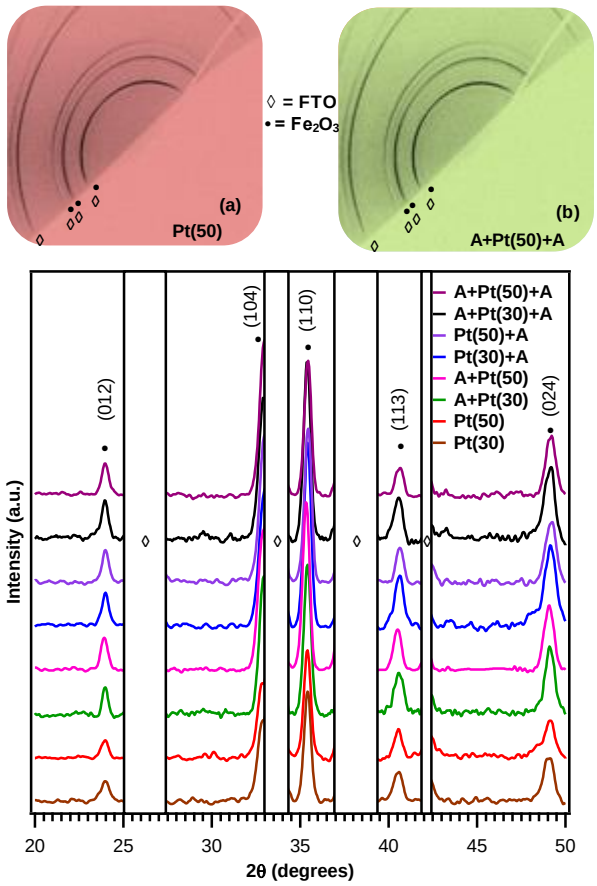


**Fig. 1** Top: XRD[2] images of two Pt/$Fe_2O_3$ samples with the highest Pt loading. Bottom: integrated XRD patterns for samples before and after thermal treatment in air. ● marks the observed α-$Fe_2O_3$ reflections. For sake of clarity, reflections pertaining to the FTO-coated glass substrate are covered and labelled by ◊.

The integrated XRD patterns of Pt/$Fe_2O_3$ systems before and after thermal treatment in air are reported in the bottom panel of Fig. 1. As can be observed, all XRD spectra are qualitatively similar and display peaks at 24.0, 33.0, 35.4, 40.6, 49.2° attributable to the (012), (104), (110), (113) and (024) *hematite* reflections.[24] A careful analysis of peak intensities evidenced that $Fe_2O_3$ crystallinity was higher in thermally treated samples than in as-prepared ones, a favorable effect for PEC applications.[1,14]

In order to investigate the system chemical composition, with particular regard to Fe and Pt oxidation states, XPS surface analyses were undertaken. In all samples, the presence of Pt, Fe and O was detected, along with a minor contribution from adventitious carbon arising from atmospheric exposure. In line with XRD results, the spectral features of the Fe2p signal (see ESI) were similar for all specimens and confirmed the presence of pure $Fe_2O_3$ free from other iron oxidation states.[5,12,15] Interestingly, XPS data provided an insightful information on the Pt chemical state, that exhibited a well evident evolution as a function of processing conditions. As a representative example, Fig. 2a displays the Pt4f signal for the as-prepared sample **Pt(50)**. In this specimen, platinum was mainly present as Pt(II)-O and Pt(IV)-O species ($Pt4f_{7/2}$ spin-orbit components located at BE = 72.6 and 74.6 eV, respectively), whereas the contribution of Pt(0) (BE = 71.3 eV) was relatively modest.[5,15,22,25] Accordingly, the O1s signal (Fig. 2b) evidenced not only the presence of *hematite* lattice oxygen (BE = 530.0 eV) and adsorbed water (BE = 533.1 eV) arising from air exposure, but also a major contribution from $PtO_x$ (x = 1,2) species at 531.4 eV.[22,26] Since no thermal treatment was carried out for this specimen, the above findings suggest that Pt was appreciably oxidized by the sole interaction with the $Fe_2O_3$ matrix, an effect likely due to the high dispersion of sputtered platinum species within *hematite* (see below).

For comparison, the Pt4f and O1s peaks for the doubly annealed specimen **A+Pt(50)+A** are reported in Fig. 2c and 2d, respectively. As can be observed, the main effect of air annealing was the increase of Pt(0) amount at expenses of Pt(IV) one, whose contribution was appreciably decreased. In line with previous works, this phenomenon can be traced back to the thermal decomposition of Pt(IV) oxide species to metallic platinum at sufficiently high temperatures.[27,28]

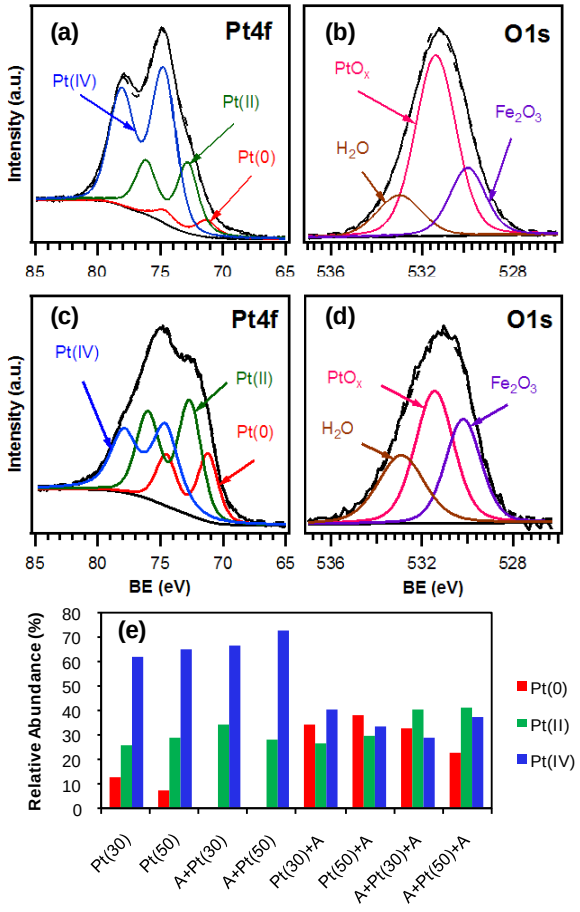


**Fig. 2** (a),(b) Deconvolution of the Pt4f and O1s surface photopeaks for the as-prepared **Pt(50)** sample. The corresponding figures for the doubly annealed specimen **A+Pt(50)+A** are shown in (c) and (d). (e) Bar diagram showing the relative abundance of Pt(0), Pt(II) and Pt(IV) species for the various Pt/$Fe_2O_3$ specimens as a function of the adopted processing conditions (compare Table 1).

A careful deconvolution of the Pt4f peak enabled to determine the relative Pt(0), Pt(II) and Pt(IV) amounts for each of the target specimens. The obtained results are summarized in Fig. 2e. As concerns the four specimens on the left side of the figure, that have not been annealed after sputtering, platinum is mainly present in its highest oxidation state Pt(IV), whereas the content of Pt(II) is relatively modest and Pt(0) contribution is even lower, or completely undetectable. In a different way, the four samples on the right side of Fig. 2e, annealed after (and, eventually, also prior to) sputtering, are characterized by an increased Pt(0) contribution at expenses of the Pt(IV) one. Such a finding unequivocally confirms the thermal decomposition of Pt(IV) oxide to metallic Pt under the used annealing conditions.[27,28]

As a final remark on XPS data, it is worth mentioning that annealing also decreased the Pt molar fraction in the sample outermost region (see Table 1). In principle, such a phenomenon could be related either to an enhanced Pt in-depth dispersion or to a surface redistribution of Pt species. In this regard, a careful analysis of FE-SEM and SIMS results (see below) highlighted that the latter phenomenon was likely the dominant one.

Fig. 3 displays the plane-view and cross-sectional FE-SEM micrographs of the as-prepared and thermally treated Pt/$Fe_2O_3$ samples obtained using a sputtering time of 50 min. Before annealing, the morphology of specimen **Pt(50)** (Fig. 3a) resembled the one of bare iron oxide.[14] Such an effect can be ascribed to the use of mild sputtering conditions and to the low platinum loading.

The iron oxide deposit was formed by dendritic structures grown perpendicularly to the substrate, whose surface appeared uniformly decorated by Pt particles of 4±1 nm. Fig. 3b displays the morphology of sample **Pt(50)+A**, subjected to air annealing after platinum sputtering. In this case the morphology of the *hematite* matrix, though more rounded close to the substrate, was still reminiscent of the pristine one (Fig. 3b *vs*. 3a), and a modest size increase of Pt NPs (7±2 nm) took place. In a different way, when annealing was performed prior to sputtering (sample **A+Pt(50)**), *hematite* underwent a remarkable morphological evolution, its texture being characterized by more rounded features and more porous than the corresponding as-prepared material (Fig. 3c *vs*. 3a). A similar topology was observed also for specimen **A+Pt(50)+A** (Fig. 3d), for which annealing was carried out even after Pt deposition. Correspondingly, a statistical analysis of FE-SEM data evidenced a slight increase of Pt NPs dimensions from 6±2 to 8±2 nm.

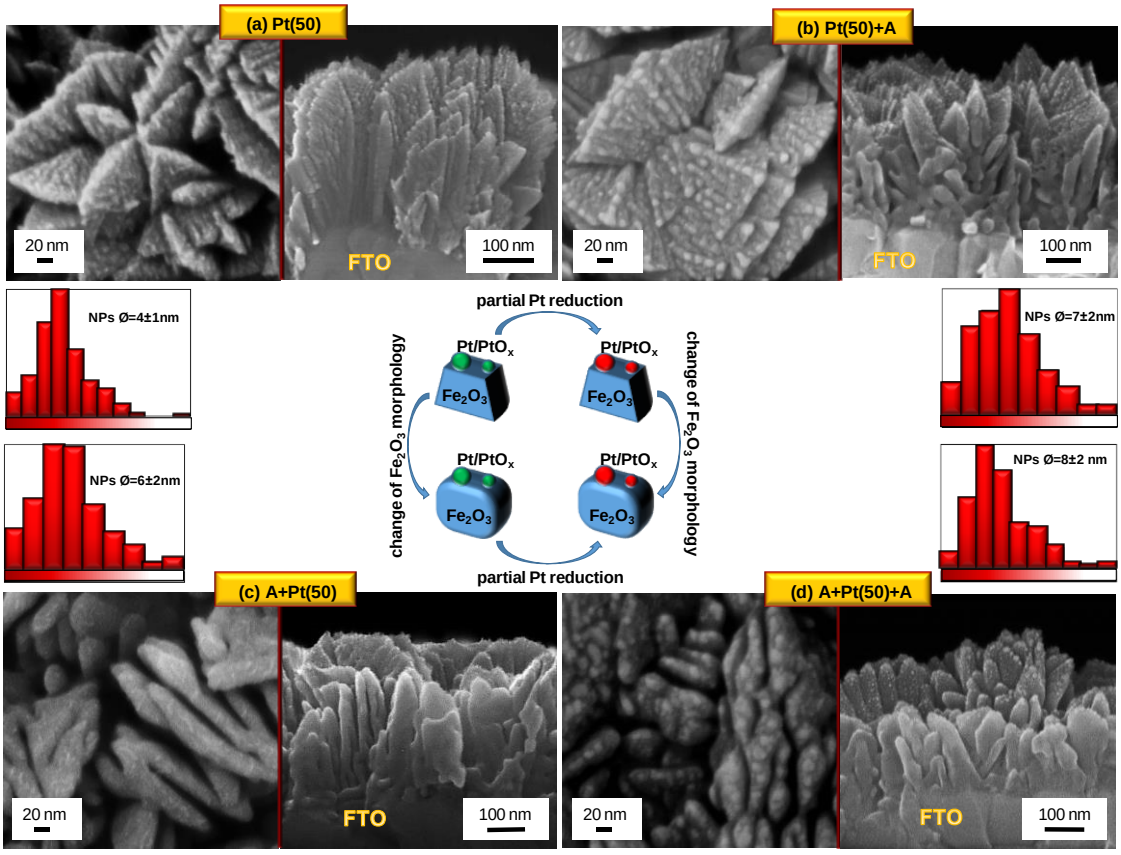


**Fig. 3** Plane-view and cross-sectional FE-SEM images of as-prepared and annealed Pt-containing $Fe_2O_3$ samples obtained with a sputtering time of 50 min. In each case, the histogram of Pt particle size distribution is also reported. The sketch at the center of the figure displays the main morphological and chemical differences between the four samples.

On the basis of the above results, the system evolution upon thermal treatment can be explained taking into account two main thermally activated phenomena: i) when annealing is performed after Pt sputtering (see Fig. 3b *vs*. 3a and 3d *vs*. 3c), the thermal energy supply promotes the decomposition of Pt(IV) oxide to Pt(0), with almost no changes of $Fe_2O_3$ morphology; ii) if annealing is carried out before sputtering on bare $Fe_2O_3$ systems (see Fig. 3c *vs*. 3a and 3d *vs*. 3b), no effect on Pt oxidation state occurs, but *hematite* morphological organization becomes more porous due to diffusion and coalescence processes. The above phenomena, detected also for samples prepared using a sputtering time of 30 min (Fig. S1, see ESI), are sketched in the central panel of Fig. 3. For all specimens, FE-SEM cross-sectional investigations enabled to estimate an average deposit thickness of 370 ± 30 nm.

In-depth SIMS analyses (Fig. 4) evidenced that, irrespective of the sputtering time and annealing conditions, Fe distribution was homogenous throughout the deposit and resulted in a sharp and well defined interface with the FTO substrate. As far as Pt is concerned, its signal decayed into the *hematite* layer with an erfchian profile.[15] Interestingly, a high Pt dispersion within the oxide matrix was observed, with a similar in-depth distribution for all samples. This phenomenon can be traced back to the adopted synthetic strategy, taking advantage of the infiltration power of the sputtering technique.[15,29] In spite of the above similarities, samples fabricated using a sputtering time of 50 min were characterized by a higher Pt content. This effect, that can be appreciated from the initial value of the Pt ionic yield (compare Fig. 4a-b with Fig. 4c-d), was confirmed by evaluating the ratio between integrals of Pt signals in different specimens, evidencing an almost doubled Pt amount upon increasing the sputtering time from 30 to 50 min. This result is in agreement with EDXS data (not reported), that revealed a Pt weight percentage of ca. 3 and 5 wt.% for sputtering times of 30 and 50 min, respectively. Finally, it is worthwhile observing that, although annealing did not enhance Pt dispersion within *hematite*, it promoted a modest Sn inter-diffusion from the FTO substrate into the *hematite* layer (Fig. 4), an effect that might positively affect charge transport phenomena, resulting in improved PEC performances.[3,8]

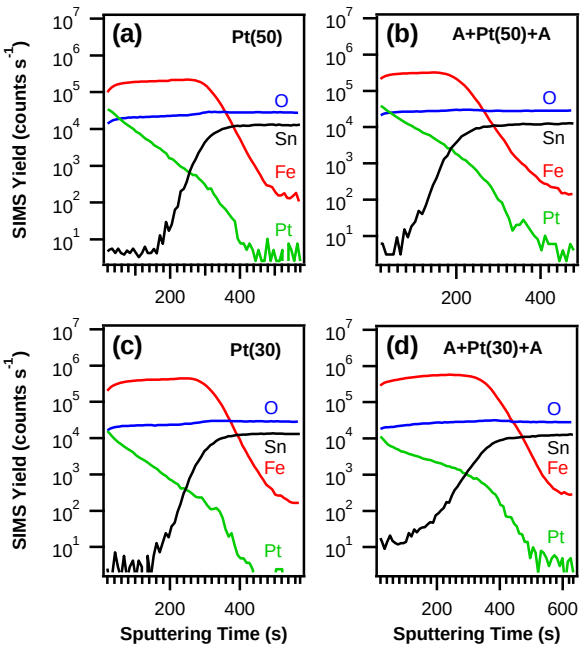


**Fig. 4** SIMS depth profiles for the as-prepared and doubly air annealed $Pt/Fe_2O_3$ specimens synthesized using a sputtering time of 50 min (a, b) and 30 min (c, d).

$Pt/Fe_2O_3$ samples were finally analyzed by optical absorption spectroscopy, that yielded similar results irrespective of platinum sputtering time. Representative absorption profiles for samples containing the highest Pt loading (50 min) are reported in Fig. 5. In agreement with previous findings on $Pt/Fe_2O_3$ nanomaterials,[13,14] Pt species did not appreciably contribute to light harvesting. As a consequence, any difference between Pt-containing specimens has to be related to the effect of air annealing on the iron oxide matrix. All specimens displayed the typical profile of *hematite* films with a sub-band-gap scattering tail in the 600-750 nm region, whose intensity increased for thermally treated samples.[8]

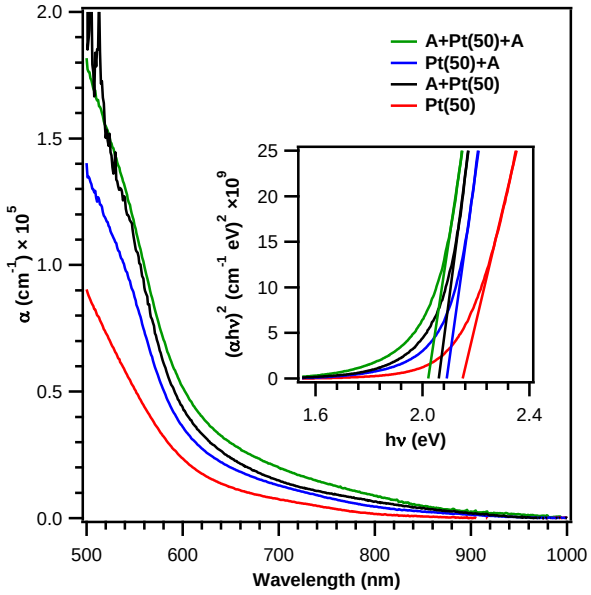


**Fig. 5** Absorption coefficient as a function of wavelength for $Pt/Fe_2O_3$ samples synthesized using a sputtering time of 50 min. The inset shows the corresponding Tauc plots.

Consistently with *hematite* band-gap transitions, a sharp raise of the absorption coefficient occurred between 500 and 600 nm, and a systematic increase of the whole spectral profile took place upon going from the as-prepared [**Pt(50)**] to the doubly annealed [**A+Pt(50)+A**] specimen. This phenomenon, along with the concomitant decrease of light penetration depth values ($\alpha^{-1}$ at $\lambda$ = 550 nm) from 200 nm [**Pt(50)**] to 90 nm [**A+Pt(50)+A**], can be traced back to a parallel enhancement of the system crystallinity, one of the key factors influencing PEC properties.[8,14] Similarly to previous works,[8] the positive effect of air annealing on light absorption properties was also confirmed by the Tauc plots reported as insets in Fig. 5, evidencing a slight decrease (ca. 0.1 eV) of band-gap values for all thermally treated samples.

PEC performances of the target materials were evaluated by measuring their current-voltage characteristics. As generally recognized, the photocurrent observed under illumination is a direct measure of the water splitting rate, reflecting the number of charge carriers produced from the incident light and their subsequent participation in water oxidation at the photoanode and hydrogen reduction at the counter-electrode.[5,9]

Journal Name

ARTICLE

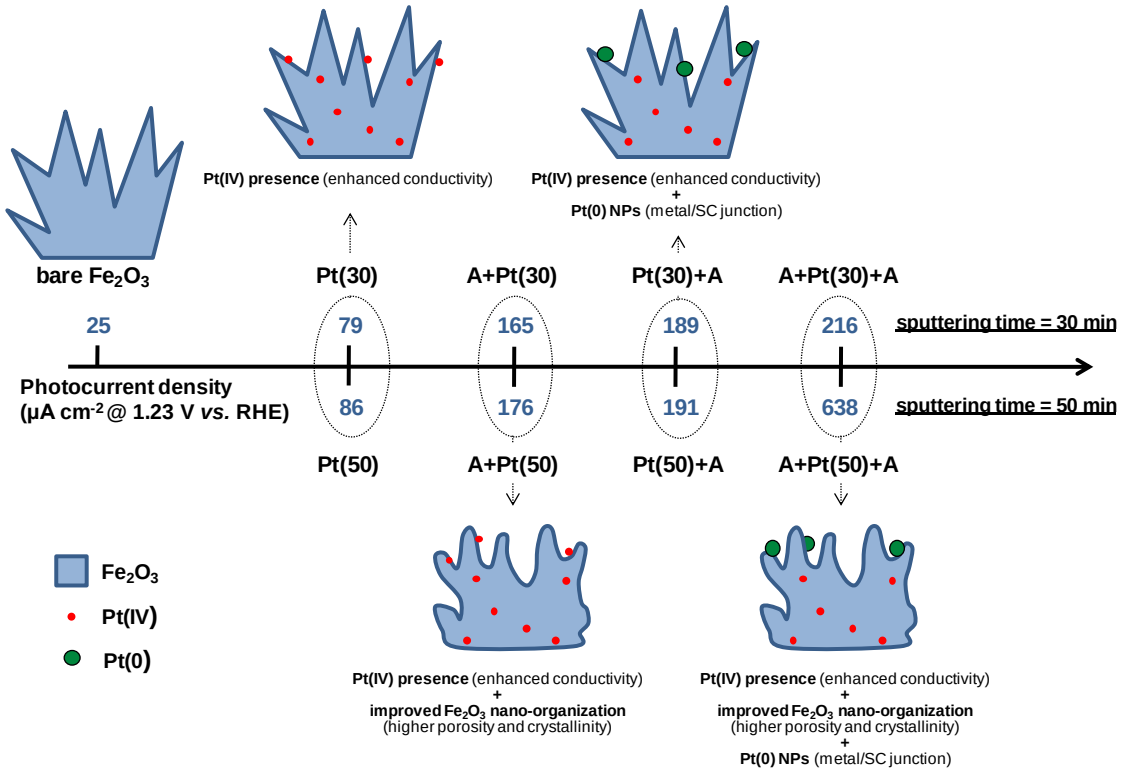


**Fig. 6** Photocurrent values at 1.23 V *vs*. RHE (the theoretical water oxidation potential) for the synthesized Pt/$Fe_2O_3$ samples, along with the corresponding bare $Fe_2O_3$ specimen.[14] The main phenomena responsible for the different PEC performances of the various samples are also sketched.

Photocurrent values at 1.23 V *vs*. RHE are summarized for all specimens in Fig. 6, where a sketch of the main phenomena responsible for the detected trends is also provided. As can be observed, photocurrent values for as-prepared specimens **Pt(30)** and **Pt(50)** were higher than those pertaining to bare $Fe_2O_3$ synthesized under the same PE-CVD conditions,[14] and slightly increased with platinum sputtering time, *i.e.* overall Pt loading in the resulting nanocomposites. This enhancement can be traced back to an increased $Fe_2O_3$ electrical conductivity and an improved charge transfer coupled with a retarded carrier recombination, related to the presence of Pt(IV) species in *hematite*-based systems.[1,5,7,9,16,17]

Interestingly, *ex-situ* thermal treatments carried out prior and/or after Pt functionalization further increased the PEC performances of Pt/α-$Fe_2O_3$ nanosystems, yielding photocurrent values strongly depended on the adopted processing conditions (Fig. 6). Basing on the above characterization data, the most important phenomena responsible for the observed photocurrent trend are described in the following. When annealing is performed *before* platinum deposition [samples **A+Pt(30)** and **A+Pt(50)**], the main difference with respect to the corresponding as-prepared systems concerns the nano-organization of iron(III) oxide. Indeed, as displayed in Figs. 3c and S1c, the *hematite* deposits show a higher porosity that anticipates an enhanced contact area with the electrolyte. Furthermore, $Fe_2O_3$ nanostructures appear more rounded and partially fused together, suggesting a lowered grain boundary content and an increased material crystallinity,[14] as also evidenced by XRD data (Fig. 1). As a whole, such effects result in a lower recombination of photogenerated charge carriers, along with an improved light absorption (Fig. 5), beneficially influencing PEC performances.[1,16,17]

In a different way, if thermal treatments are carried out *after* Pt sputtering [samples **Pt(30)+A** and **Pt(50)+A**], photocurrents are further increased compared to the corresponding as-prepared heterocomposites (Fig. 6). In this case, Figs. 3b and S1b indicate that $Fe_2O_3$ morphology resembles rather closely that of samples prior to annealing. As a consequence, the improved PEC performances should be mainly related to variations in the platinum oxidation state. In fact, XPS data (see Fig. 2) clearly indicated that post-annealing resulted in the thermal decomposition of Pt(IV) oxide to Pt(0) species, whose presence can favour $e^-/h^+$ separation and increase photohole lifetime.[4,5,13,30] In an attempt to carry out a complete reduction of Pt-containing species to metallic platinum, hydrogen plasma treatments were carried out and the results are discussed in detail in the ESI section.

Regarding samples subjected to annealing both *before* and *after*

platinum deposition [**A+Pt(30)+A**, **A+Pt(50)+A**], their functional performances synergistically benefitted from all the above described phenomena and, in fact, they presented the best PEC behavior in the whole series (Fig. 6). To better appreciate this effect, Fig. 7 reports the photocurrent density *vs.* applied potential curves for Pt/α-$Fe_2O_3$ nanosystems characterized by the higher (Fig. 7a) and the lower (Fig. 7b) Pt loading, comparing the photoresponses of as-prepared samples [**Pt(30)**, **Pt(50)**] against those of the doubly annealed ones [**A+Pt(30)+A**, **A+Pt(50)+A**].

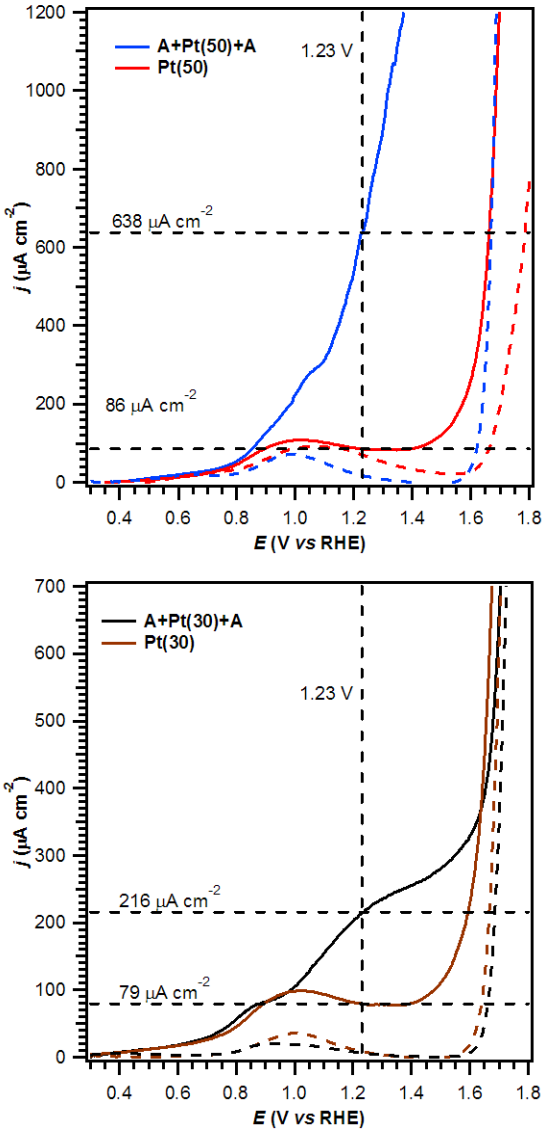


**Fig. 7** Photocurrent density *vs*. applied potential curves for selected Pt/α-$Fe_2O_3$ specimens obtained with a sputtering time of 50 min (a) and 30 min (b). Sample labeling as in Table 1. Continuous and dotted curves were collected under light and dark conditions, respectively.

As can be observed, irrespective of Pt deposition time, photocurrent values measured under light irradiation (continuous curves) at 1.23 V *vs*. RHE underwent an appreciable increase upon thermal treatment. Nevertheless, dark current measurements (dotted curves) displayed a current onset at about 1.6 V *vs.* RHE, indicating that no appreciable contributions from water electrolysis took place at 1.23 V.

In particular, the significant photocurrent increase occurring for sample **A+Pt(50)+A** with respect to the **Pt(50)** one (Fig. 7a) indicated that a much larger number of photocarriers participated to water splitting.[5] In this case, the absence of any saturation *plateau* at more positive potentials evidenced an efficient charge separation upon illumination,[11] indicating that PEC performances improved with Pt content.

Remarkably, the photoefficiency of the **A+Pt(50)+A** specimen was higher than that reported for bare $Fe_2O_3$ photoelectrodes,[3,8,20,23,31-37] and compared favourably not only with *hematite* films variously doped [6,38-42] or functionalized,[23,30,43-45] but also with previous Pt-containing $Fe_2O_3$ materials.[7,9,11,17] Hence, the present Pt/$Fe_2O_3$ nanosystems stand as promising candidates for practical utilization in PEC cells.

In order to gain a deeper insight into the above discussed PEC performances and to investigate the dynamics of photogenerated charge carriers, TAS analyses were undertaken on samples **Pt(50)** and **A+Pt(50)+A**. These specimens were chosen as representative taking into account that they present the highest photocurrent variation and, in the case of sample **A+Pt(50)+A**, the best photoresponse recorded in the whole analyzed set. Dynamics of photogenerated charge carriers following the band-gap photoexcitation at 355 nm were examined by using ps and ms transient absorption spectroscopy. As shown in the following, the analyses enabled to determine recombination time constants (τ) of photogenerated charge carriers in the target photoanodes. It is worth remembering that time constants represent intrinsic electron-hole characteristics of the material (fs-ns timescale) and the OER reaction rate at the SCLJ (ms-s timescale), and hence have a direct interrelation with the system photoactivity.

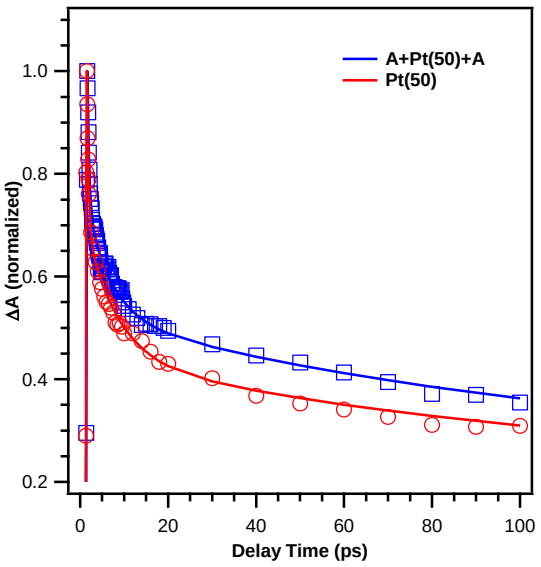


**Fig. 8** Normalized ultrafast transient absorption decays of Pt/$Fe_2O_3$ specimens measured at a probe wavelength of 650 nm. The solid lines represent exponential fits of the raw data.

TAS experiments in a ps time resolution were performed to investigate intrinsic charge carrier recombination characteristics following the excitation laser pulse. A probe wavelength of 650 nm was selected for data elaboration, as it represents the value at which the maximum photohole amplitude is observed in *hematite*.[18] Fig. 8 displays normalized absorption decay profiles of the as-prepared and doubly annealed Pt/α-$Fe_2O_3$ specimens on a 0-

100 ps timescale. A four-exponential fitting procedure was required to obtain a reasonable fit quality, demonstrating the complex decay nature of photoinduced charges in *hematite* photoanodes in the ultra-fast time range. Time constants of 0.1, 1.9, 60, and 5500 ps and 0.4, 5.6, 115, and 7500 ps were obtained for samples **Pt(50)** and **A+Pt(50)+A**, respectively, showing the intrinsically rapid electron-hole recombination. The three fastest time constants, similar to those previously reported, are attributed to hot carrier cooling, free electron recombination, and surface trapping.[46] The fourth long-lived component corresponds to holes surviving for nanoseconds or more, due to electron trapping to the mid-gap traps of *hematite*, with a sufficiently prolonged lifetime to facilitate the OER reaction. The sample subjected to thermal treatment experienced a decreased charge carrier recombination rate ($1/\tau$) providing an enhanced photohole lifetime, as illustrated in Fig. 8. These results highlight the key role of air annealing to achieve enhanced PEC performances.

Transient absorption traces for the above Pt/α-$Fe_2O_3$ specimens in a ms timescale are shown in Fig. S6 (see ESI). Annealing enhanced charge carrier lifetime also in a ms timescale, as confirmed by the recombination time constants obtained by bi-exponential fitting (5 *vs.* 22 ms and 140 *vs.* 4200 ms for samples **Pt(50)** and **A+Pt(50)+A**, respectively) of the decay profiles. Hence, lifetime of photoholes is extended to a second time range upon annealing of Pt/α-$Fe_2O_3$, a key necessity for efficient water oxidation.[47]

As a whole, basing on the above results, the prolonged lifetime detected for the doubly annealed specimen both in the ps and ms timescale can be attributed to the concomitance of some main effects: i) the enhanced $Fe_2O_3$ conductivity and improved charge transfer, related to the presence of Pt(IV) species;[7,9] ii) the improved *hematite* porosity and crystallinity, coupled with a more efficient light absorption;[18,19] iii) the presence of Pt(0) aggregates at the $Fe_2O_3$ surface, that may favour $e^-/h^+$ separation.[4,5,13]

## Conclusions

In summary, high purity Pt/α-$Fe_2O_3$ nanosystems have been prepared by means of an hybrid synthetic route, consisting of PE-CVD of $Fe_2O_3$ deposits on FTO followed by sputtering of platinum and eventual *ex-situ* annealing in air.

The obtained as-prepared materials were formed by iron oxide dendritic nanostructures that, thanks to the sputtering infiltration power, were efficiently decorated by oxidized platinum species. Interestingly, simple variations of the thermal treatment procedure allowed a fine control of iron oxide nano-organization, as well as of platinum redox chemistry, strongly affecting the system efficiency in PEC water splitting. In particular, depending on the adopted processing conditions, annealing promoted an increase of *hematite* porosity, crystallinity, as well as light absorption properties, and/or the partial reduction of oxidized platinum species to Pt(0). The synergic combination of such favourable effects allowed to maximize PEC performances yielding photocurrent values as high as 638 μA $cm^{-2}$ at 1.23 V *vs*. RHE.

Overall, the results provided herein pave the way to the engineering of *hematite*-based nanosystems as efficient photoanodes for the conversion of radiant into chemical energy. Nevertheless, to take full advantage of the present heterocomposites, it is of utmost importance to master their nanoscale assembly into targeted three-dimensional structures, possibly characterized by lower nanostructure size (*i.e.* closer to the hole diffusion length). Further work in this direction, as well as in understanding the exact role of Pt functionalization on the surface states, mechanism and PEC behavior of *hematite* nanosystems, will undoubtedly be of key importance. To this aim, future research efforts will be dedicated to a deeper investigation of charge transfer phenomena also by impedance spectroscopy. Finally, the modification of the present Pt/α-$Fe_2O_3$ photoelectrode materials with catalytic/plasmonic NPs or surface passivation layers (e.g. Co-Pi, Au, $TiO_2$) will also be explored to further increase PEC performances.

## Acknowledgements

The research leading to these results has received funding from the FP7 project "SOLAROGENIX" (NMP4-SL-2012-310333), as well as from Padova University ex-60% 2012-2014 projects, grant n°CPDR132937/13 (SOLLEONE), and Regione Lombardia-INSTM ATLANTE projects.

## References

1. J. Y. Kim, G. Magesh, D. H. Youn, J.-W. Jang, J. Kubota, K. Domen and J. S. Lee, *Sci. Rep.*, 2013, **3**, 2681.
2. L. Li, P. A. Salvador and G. S. Rohrer, *Nanoscale*, 2014, **6**, 24-42.
3. Y. Ling, G. Wang, D. A. Wheeler, J. Z. Zhang and Y. Li, *Nano Lett.*, 2011, **11**, 2119-2125.
4. S. Linic, P. Christopher and D. B. Ingram, *Nat. Mater.*, 2011, **10**, 911-921.
5. A. Mao, N.-G. Park, G. Y. Han and J. H. Park, *Nanotechnol.*, 2011, **22**, 175703.
6. H. K. Dunn, J. M. Feckl, A. Muller, D. Fattakhova-Rohlfing, S. G. Morehead, J. Roos, L. M. P. Peter, C. Scheu and T. Bein, *Phys. Chem. Chem. Phys.*, 2014, **16**, 24610-24620.
7. G. Rahman and O.-S. Joo, *Mater. Chem. Phys.*, 2013, **140**, 316-322.
8. K. Sivula, R. Zaboril, F. L. Formal, R. Robert, A. Weidenkaff, J. Tucek, J. Frydrych and M. Grätzel, *J. Am. Chem. Soc.*, 2010, **132**, 7436-7444.
9. Y.-S. Hu, A. Kleiman-Shwarsctein, A. J. Forman, D. Haxen, J.-N. Park and E. W. McFarland, *Chem. Mater.*, 2008, **20**, 3803-3805.
10. T. J. LaTempa, X. Feng, M. Paulose and C. A. Grimes, *J. Phys. Chem. C*, 2009, **113**, 16293-16298.
11. S. Shen, M. Li, L. Guo, J. Jiang and S. S. Mao, *J. Coll. Interface Sci.*, 2014, **427**, 20-24.
12. A. Mettenbörger, T. Singh, A. P. Singh, T. T. Järvi, M. Moseler, M. Valldor and S. Mathur, *Int. J. Hydrogen Energy*, 2014, **39**, 4828-4835.
13. H. Liang, X. Jiang, W. Chen, S. Wang, B. Xu and Z. Wang, *Ceramics International*, 2014, **40**, 5653-5658.
14. M. E. A. Warwick, K. Kaunisto, D. Barreca, G. Carraro, A. Gasparotto, C. Maccato, E. Bontempi, C. Sada, T.-P. Ruoko, S. Turner and G. Van Tendeloo, *ACS Appl. Mater. Interfaces*, 2015, DOI: 10.1021/acsami.1025b00919.
15. G. Carraro, D. Barreca, E. Comini, A. Gasparotto, C. Maccato, C. Sada and G. Sberveglieri, *CrystEngComm*, 2012, **14**, 6469-6476.
16. H. G. Cha, J. Song, H. S. Kim, W. Shin, K. B. Yoon and Y. S. Kang, *Chem. Comm.*, 2011, **47**, 2441-2443.
17. Y.-P. Hsu, S.-W. Lee, J.-K. Chang, C.-J. Tseng, K.-R. Lee and C.-H. Wang, *Int. J. Electrochem. Sci.*, 2013, **8**, 11615-11623.
18. M. Barroso, S. R. Pendlebury, A. J. Cowan and J. R. Durrant, *Chem. Sci.*, 2013, **4**, 2724-2734.

19. S. R. Pendlebury, A. J. Cowan, M. Barroso, K. Sivula, J. Ye, M. Grätzel, D. R. Klug, J. Tang and J. R. Durrant, *Energy Environ. Sci.*, 2012, **5**, 6304-6312.
20. D. Barreca, G. Carraro, A. Gasparotto, C. Maccato, C. Sada, A. P. Singh, S. Mathur, A. Mettenbörger, E. Bontempi and L. E. Depero, *Int. J. Hydrogen Energy*, 2013, **38**, 14189-14199.
21. D. Barreca, G. Carraro, A. Devi, E. Fois, A. Gasparotto, R. Seraglia, C. Maccato, C. Sada, G. Tabacchi, E. Tondello, A. Venzo and M. Winter, *Dalton Trans.*, 2012, **41**, 149-155.
22. J. F. Moulder, W. F. Stickle, P. E. Sobol and K. D. Bomben, *Handbook of X-ray Photoelectron Spectroscopy*, Perkin Elmer Corperation, Eden Prairie, MN, USA, 1992.
23. O. Zandi, J. A. Beardslee and T. Hamann, *J. Phys. Chem. C*, 2014, **118**, 16494-16503.
24. Pattern N° 33-0664 JCPDS (2000)
25. A. S. Aricò, A. K. Shukla, H. Kim, S. Park, M. Min and V. Antonucci, *Appl. Surf. Sci.*, 2001, **172**, 33-40.
26. http://srdata.nist.gov/xps
27. L. K. Ono, B. Yuan, H. Heinrich and B. Roldan Cuenya, *J. Phys. Chem. C*, 2010, **114**, 22119-22133.
28. A. Mosquera, D. Horwat, L. Vazquez, A. Gutierrez, A. Erko, A. Anders, J. Andersson and J. L. Endrino, *J. Mater. Res.*, 2012, **27**, 829-836.
29. G. Carraro, A. Gasparotto, C. Maccato, E. Bontempi, F. Bilo, D. Peeters, C. Sada and D. Barreca, *CrystEngComm*, 2014, **16**, 8710-8716.
30. E. Thimsen, F. Le Formal, M. Grätzel and S. C. Warren, *Nano Lett.*, 2011, **11**, 35-43.
31. T. W. Hamann, *Dalton Trans.*, 2012, **41**, 7830-7834.
32. Z. Fu, T. Jiang, Z. Liu, D. Wang, L. Wang and T. Xie, *Electrochim. Acta*, 2014, **129**, 358-363.
33. J. Liu, M. Shahid, Y.-S. Ko, E. Kim, T. K. Ahn, J. H. Park and Y.-U. Kwon, *Phys. Chem. Chem. Phys.*, 2013, **15**, 9775-9782.
34. J. Liu, Y. Y. Cai, Z. F. Tian, G. S. Ruan, Y. X. Ye, C. H. Liang and G. S. Shao, *Nano Energy*, 2014, **9**, 282-290.
35. S. C. Riha, B. M. Klahr, E. C. Tyo, S. Seifert, S. Vajda, M. J. Pellin, T. W. Hamann and A. B. F. Martinson, *ACS Nano*, 2013, **7**, 2396-2405.
36. L. Jia, K. Harbauer, P. Bogdanoff, I. Herrmann-Geppert, A. Ramirez, R. van de Krol and S. Fiechter, *J. Mater. Chem. A*, 2014, **2**, 20196-20202.
37. R. Rajendran, Z. Yaakob, M. Pudukudy, M. S. A. Rahaman and K. Sopian, *J. All. Compounds*, 2014, **608**, 207-212.
38. I. Cesar, K. Sivula, A. Kay, R. Zboril and M. Grätzel, *J. Phys. Chem. C*, 2009, **113**, 772-782.
39. S. Shen, C. Kronawitter, J. Jiang, S. Mao and L. Guo, *Nano Res.*, 2012, **5**, 327-336.
40. J. Liu, C. Liang, G. Xu, Z. Tian, G. Shao and L. Zhang, *Nano Energy*, 2013, **2**, 328-336.
41. S. Kumari, A. P. Singh, Sonal, D. Deva, R. Shrivastav, S. Dass and V. R. Satsangi, *Int. J. Hydrogen Energy*, 2010, **35**, 3985-3990.
42. A. Kleiman-Shwarsctein, Y.-S. Hu, A. J. Forman, G. D. Stucky and E. W. McFarland, *J. Phys. Chem. C*, 2008, **112**, 15900-15907.
43. M. Tallarida, C. Das, D. Cibrev, K. Kukli, A. Tamm, M. Ritala, T. Lana-Villarreal, R. Gómez, M. Leskelä and D. Schmeisser, *J. Phys. Chem. Lett.*, 2014, 3582-3587.
44. L. Fu, H. Yu, C. Zhang, Z. Shao and B. Yi, *Electrochim. Acta*, 2014, **136**, 363-369.
45. S. Shen, *J. Mater. Res.*, 2014, **29**, 29-46.
46. J. B. Baxter, C. Richter and C. A. Schmuttenmaer, *Annu. Rev. Phys. Chem.*, 2014, **65**, 423-447.
47. A. J. Cowan, C. J. Barnett, S. R. Pendlebury, M. Barroso, K. Sivula, M. Grätzel, J. R. Durrant and D. R. Klug, *J. Am. Chem. Soc.*, 2011, **133**, 10134-10140.